

Demonstration of shift, scale, and rotation invariant target recognition using polar Mellin transforms in a hybrid opto-electronic correlator

Julian Gamboa

Department of ECE, Northwestern University, Evanston, IL, 60208, USA

Mohamed Fouda

Department of ECE, Northwestern University, Evanston, IL, 60208, USA

Stephen M. Johnson

Department of ECE, Northwestern University, Evanston, IL, 60208, USA

Selim M. Shahriar

Department of ECE, Northwestern University, Evanston, IL, 60208, USA

Department of Physics and Astronomy, Northwestern University, Evanston, IL, 60208, USA

Abstract: A hybrid opto-electronic correlator (HOC), previously proposed by us, can achieve the functionality of a holographic optical correlator without requiring the use of holograms. In this paper, we describe the results of our experimental demonstration of the scale, rotation and shift invariance of the HOC, employing polar Mellin transformed (PMT) versions of images. The correlation signal can be used to determine the relative scale and angular orientation of the original images. A pair of spatial light modulators (SLMs) was used for applying the PMT transformed versions of the reference and object images in this demonstration. For searching through a large database using the HOC, one can use, for the reference arm, a high-capacity thick holographic memory device. We describe the practical design of such a device made using phenanthrenequinone dye embedded in a poly-methyl-methacrylate (PMMA) substrate.

1. INTRODUCTION

An important aspect of space situational awareness (SAS) is the monitoring of ground sites involved in controlling space vehicles and activities, using unmanned aerial vehicles or space platforms. For this type of surveillance, it is necessary to recognize objects in a speedy and robust manner. Of special interest are optical image recognition systems, which generally present faster processing speeds over traditional electronics-based systems. One example of such a system is the Vander Lugt correlator [1–3], which uses holographic filters to compare two images. This system, while useful, finds its key limitation in having a slow recording process for the filters. Other correlators have employed alternative configurations in order to avoid the recording process altogether, such as the joint transform correlator (JTC) [4–9], which uses dynamic materials that are able to produce correlations in real time. Nonetheless, these materials suffer from many practical problems, such as needing to be exposed to high voltages, which can often irreparably damage them [10,11]. We recently proposed and demonstrated the hybrid opto-electronic correlator (HOC) [12,13] that overcomes these limitations by replacing the JTC's nonlinear material with detectors. This system is naturally shift invariant, but is sensitive to changes in scale and rotation. There have been many proposals to overcome these limitations, many of which entail the implementation of coordinate transforms [14–18]. We have also shown that by incorporating the polar Mellin transform (PMT), the HOC is capable of shift, rotation, and scale invariance [19,20]. The next step for fully automating the HOC is to incorporate a thick holographic memory device (HMD) for large database storage. Such a device would be able to reduce the electronic components of the HOC and increase its potential correlation speeds. In this paper, we detail and analyze the correlation process of the PMT-enhanced HOC, as well as the development of an HMD based on phenanthrenequinone (PQ) dye embedded in a poly-methyl-methacrylate (PMMA) substrate.

The rest of the paper is organized as follows. Section 2 details the experimental setup and theory of operation of the HOC. An overview of the steps required to implement the PMT in the HOC is given in section 3. The results are presented and examined in section 4, where we show how the use of the PMT conforms to the theory. Progress towards the incorporation of holographic storage into the HOC is discussed in section 5. We conclude with the summary and outlook in section 6.

2. THEORY BEHIND THE HOC

The details of the basic HOC architecture can be found in [12] and [13], while the augmentation thereof via incorporation of the PMT can be found in [20]. The first practical demonstration of the augmented HOC is given in [19]. In its current form, the operating speed of the HOC is limited due to the use of commercial electronic devices and the serial communication between them. To remedy this, we have proposed a system called the integrated graphic processing unit (IGPU) which may allow the HOC to perform a correlation in a time scale as short as few microseconds [12,19,20]. Furthermore, it is possible to implement an HMD into one arm of the HOC as a mass storage device to both speed up and simplify the architecture. While much work remains to be done before the IGPU can be created, we have begun development of the HMD.

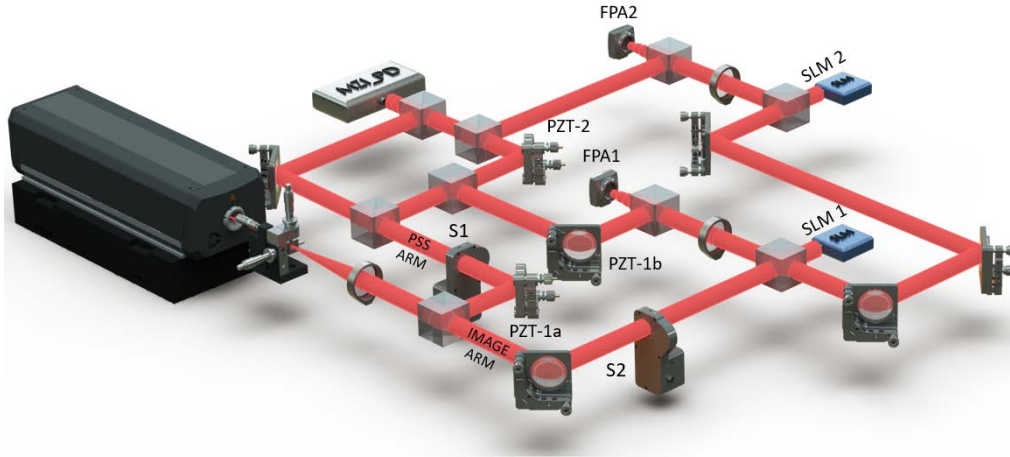


Fig 1. Simplified architecture of the HOC for demonstrating the working principle using the PMT, shutters, and SLM's.

2.1 OVERVIEW OF THE PMT AUGMENTED HOC

Like other optical correlators, the HOC takes advantage of the Fourier transform (FT) property of lenses. However, unlike traditional holographic correlators, it does not require a writing step where the information of the FT of the reference image is stored prior to its operation. Instead, the HOC captures the FT of the reference and query images, at the same time, on two separate arms. A Focal Plane Array (FPA) on each arm captures three intensity signals: the FT of the image, an auxiliary plane wave, and the interference between these two. The amplitude and phase information for the FT of the image is thus captured for each arm. We then subtract the intensity of the FT'd image beam and the auxiliary plane wave from the interference pattern for each arm. This yields two electronic FT-domain signals that are then multiplied together, pixel-by-pixel. By transferring this signal back to the optical domain using a spatial light modulator (SLM), we can pass it through another lens and obtain its FT, which correspond to the space-domain convolution and correlation of the two original images. This is explained in greater details in Section 2.3. The amplitudes of the cross-correlation and convolution produced this way depend on the relative phase of the two auxiliary plane waves. Thus, for a practical implementation of this scheme we employ a Phase Stabilizer and Scanner (PSS), which is described in more details in Section 2.4.

The process as described above is able to recognize a match between a reference image and a query image in a shift invariant manner. However, it is not rotation and scale invariant. This limitation is eliminated by employing the PMT process. This involves the following additional steps in each arm before the interference with the auxiliary beams occurs. First, the FT of each image is detected with an FPA, then the amplitude of the FT is determined by taking the square root of the signal for each pixel. The resulting numbers are then converted from the rectilinear coordinates $\{x,y\}$ to a polar coordinate $\{r,\theta\}$, by using the relation $\theta = \tan^{-1}(y/x)$ and $r = (x^2 + y^2)^{1/2}$. The values of the signal are then represented in a two-dimensional rectilinear array, where r and θ form the two orthogonal coordinates. In order to carry out this mapping, it is necessary to exclude the information in a small circle around the center of the amplitude of the FT. The radius of this circle, r_0 , is chosen to be small enough to ensure that important

features in the image are not lost. Finally, we map the signals from the $\{r, \theta\}$ array to a $\{\rho, \theta\}$ array, where $\rho = \ln(r/r_0)$. This is the array that is interfered with the auxiliary beam in each arm. More details of this process can be found in [20].

2.2 EXPERIMENTAL SETUP

For this demonstration we have used the architecture illustrated schematically in Fig. 1, more details about which can be found in [19]. A continuous-wave diode-pumped solid-state laser (Verdi V2) at 532 nm is used as the light source. The laser beam starts with a diameter of 1mm, which is spatially filtered and expanded to 1" (25.4 mm). This beam is passed through a 50/50 Beam Splitter (BS) into two arms; the Image Arm and the PSS Arm. The latter leads to a mirror mounted on a Piezo-electric Transducer (PZT-1a) which redirects the beam through a shutter (S1) to a Mach-Zehnder Interferometer (MZI). The MZI, along with PZT-2, a pair of photo-detectors (MZI PD) that are separated to detect two different fringes in the MZI interference pattern, and a Proportional-Integral-Differential (PID) controller, forms a phase-stabilization system. This MZI has two BS's inserted in one path. These redirect two plane waves (C_1, C_2) towards the image arms, with C_1 passing through PZT-1b. The phase-stabilization system allows us to lock the phase difference between C_1 and C_2 according to a bias voltage applied to the output of the PID controller. This is discussed in greater detail in Section 2.4. The image arm also passes through a shutter (S2) and is then split into the reference and query arms. Each of these two beams reflects off an amplitude modulated (AM) SLM to produce the image beams (H_1, H_2), each of which is then directed towards a biconvex lens. The lens produces the two-dimensional FT of the image at its focal plane. Each of the FT'd image beams (M_1, M_2) then interferes with the corresponding plane wave prior to being detected by an FPA placed at the focal distance of the biconvex lens. For this setup we used the Thorlabs USB2.0 CMOS camera (DCC1545M), which has a resolution of 1280x1024 pixels, to perform the function of the FPA.

The use of shutters allows us to choose what we detect. We can detect just the FT'd image beams ($B = |M|^2$) by closing S1 and opening S2; just the plane waves ($|C|^2$) by opening S1 and closing S2; or the interference patterns ($A = |M + C|^2$) by opening both shutters. The SLM's used for this demonstration are custom-made using Texas Instrument's DLP3000 modules. These make use of Digital Micro-mirror Devices (DMD's) which rapidly move to reflect light towards and then away from a target, effectively functioning as amplitude modulated SLM's. The DLP3000 modules have a physical resolution of 684 x 608 pixels, but operate in a wide aspect ratio of 854 x 480. Each individual micro-mirror measures 7.6 μm across.

2.3 MATHEMATICAL MODEL OF THE HOC

Each set of measurements (A_j, B_j , and C_j ; where $j=1,2$) is taken by opening and closing the shutters as described in the previous section, using the subscript '1' to denote the reference image, and the subscript '2' for the query. The FT of each image and each plane wave can be expressed as follows:

$$M_j = |M_j| \exp(i\phi_j); \quad C_j = |C_j| \exp(i\Psi_j) \quad (1)$$

where $\phi_j(x, y)$ is the phase of the FT'd image beam at the FPA plane, and Ψ_j is the phase of the interfering plane wave at the same point. Here, $|M_j|$ and ϕ_j are functions of (x, y) , but $|C_j|$ and Ψ_j are assumed to be constant on the FPA plane. The detected interference pattern between the FT of the image (M_j) and the plane wave (C_j) is given by:

$$\begin{aligned} A_j &= |M_j + C_j|^2 \\ &= |M_j|^2 + |C_j|^2 + |M_j||C_j| \left(\exp(i[\phi_j - \Psi_j]) + \exp(-i[\phi_j - \Psi_j]) \right) \end{aligned} \quad (2)$$

This digital signal array can be stored on an FPGA along with the signal arrays B_j and $|C_j|^2$. The FPGA can then perform a subtraction to obtain:

$$\begin{aligned} S_j &= A_j - B_j - C_j \\ &= |M_j||C_j| \left(\exp(i[\phi_j - \Psi_j]) + \exp(-i[\phi_j - \Psi_j]) \right) \\ &= M_j C_j^* + M_j^* C_j \end{aligned} \quad (3)$$

This signal can be stored for both the reference (S_1) and the query (S_2) image in the same FPGA and later multiplied together using four-quadrant multiplication to find the signal array S :

$$\begin{aligned}
S &= S_1 \times S_2 \\
&= (M_1 C_1^* + M_1^* C_1) \times (M_2 C_2^* + M_2^* C_2) \\
&= \alpha^* M_1 M_2 + \alpha M_1^* M_2^* + \beta^* M_1 M_2^* + \beta M_1^* M_2
\end{aligned} \tag{4}$$

where $\alpha = C_1 C_2$, $\beta = C_1 C_2^*$.

The resulting signal can be sent to an SLM to be transferred into the optical domain using a laser. Here, the signal beam can be FT'd by passing through a biconvex lens, presenting the final output signal S_f at the focal plane:

$$\begin{aligned}
S_f &= \mathcal{F}\{S\} \\
&= \alpha^* \mathcal{F}\{M_1 M_2\} + \alpha \mathcal{F}\{M_1^* M_2^*\} + \beta^* \mathcal{F}\{M_1 M_2^*\} + \beta \mathcal{F}\{M_1^* M_2\}
\end{aligned} \tag{5}$$

Here \mathcal{F} stands for the FT. Because M_j is the FT of an image H_j , we can now use the well-known relationship between the FT of products of functions and convolutions and cross-correlations to express more explicitly the four terms in S_f :

$$\begin{aligned}
S_f &= \alpha^* T_1 + \alpha T_2 + \beta^* T_3 + \beta T_4 \\
T_1 &= H_1(x, y) \otimes H_2(x, y) \\
T_2 &= H_1(-x, -y) \otimes H_2(-x, -y) \\
T_3 &= H_2(x, y) \odot H_1(x, y) \\
T_4 &= H_1(x, y) \odot H_2(x, y)
\end{aligned} \tag{6}$$

where \otimes indicates two-dimensional convolution, and \odot indicates two-dimensional cross-correlation. This shows that using three intensity signals (A, B, and C) from each arm we can find the correlation between the two images. In Eqs. (4) to (6) we have grouped together the factors corresponding to the plane waves C_1 and C_2 into constants (α and β). A more explicit expression of these terms reveals the following:

$$\alpha = C_1 C_2 = |C_1| |C_2| \exp(i(\Psi_1 + \Psi_2)) \tag{7}$$

$$\beta = C_1 C_2^* = |C_1| |C_2| \exp(i(\Psi_1 - \Psi_2)) \tag{8}$$

It is clear that the output of the HOC depends nontrivially on the phases of the plane waves at their respective FPA's. We are also only interested in the cross-correlation terms of our output signal (T_3 and T_4); as such it is our goal to maximize $|\beta|$ and minimize α while maintaining both values stable. For this we have designed and implemented a PSS that is explained in the next section.

2.4 PHASE STABILIZATION AND SCANNING

The PSS can be considered to be a specific type of optical phase-locked loop (OPLL) with the added phase scan. Currently there are very few ways to implement a stable OPLL [21–23], and integrated circuits that perform this task are still at the research stage. To overcome this problem, we designed a discreet OPLL that can maintain lock for some time, along with a method of quickly reestablishing optimum lock values. The HOC requires us to control the phase difference between our Reference and Query auxiliary plane waves.

From Eq. (8) it is clear that $|\beta|$ will reach its maximum value when $\Psi_1 - \Psi_2 = 2\pi m$, where m is an integer. In order to achieve such a value, the HOC architecture incorporates an MZI with an adjustable mirror (PZT-2) and two coupled detectors (MZI PD), as shown in Fig. 2, which is a different view of the apparatus shown in Fig. 1. These detectors are separated a short distance on the plane normal to the direction of propagation of the laser, which allows them to detect different fringes of the interference pattern generated in the MZI. An electronic circuit finds the difference in intensity between these detectors and converts it into a voltage that is then fed into a low noise pre-amp and then a PID controller. The output of the PID is then added to a bias voltage that allows us to control the locking point before being connected to PZT-2. This system operates under the assumption that the mirrors and the optical path lengths are very stable. For this reason, the optical table is floated and the experiment is enclosed so as to minimize air turbulence.

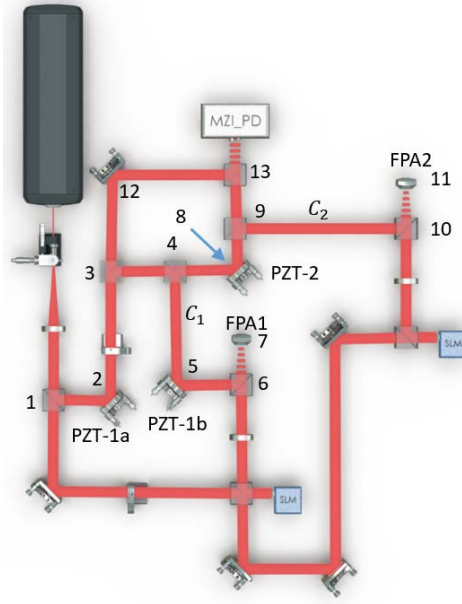


Fig 2. HOC diagram. The numbers represent vertices used to describe path lengths.

The first plane wave (C_1) is extracted from the MZI prior to the PZT, having travelled a distance L_{c1} from the first BS to FPA-1a, given by:

$$L_{c1} = l_{1,2} + l_{2,3} + l_{3,4} + l_{4,5} + l_{5,6} + l_{6,7} \quad (9)$$

where $l_{m,n}$ indicates the path from element m to element n . The second plane wave (C_2) is extracted after PZT-2. The total path length for this plane wave from the first BS to FPA-2 is L_{c2} , given by:

$$L_{c2} = l_{1,2} + l_{2,3} + l_{3,4} + l_{4,8} + l_{8,9} + l_{9,10} + l_{10,11} \quad (10)$$

PZT-2 allows us to change $[l_{4,8} + l_{8,9}]$ via the bias voltage, thus extending or shortening L_{c2} . Without considering the effects of the optical components (BS's and mirrors) which produce constant phase shifts, the phase of each plane wave can be written as:

$$\Psi_j = k \times L_{c_j}; \quad k = 2\pi / \lambda$$

Using this expression, we can now find the phase difference to be:

$$\begin{aligned} \Delta\Psi &= \Psi_1 - \Psi_2 = k \times (L_{c1} - L_{c2}) + \Delta\phi_{OE} \\ &= k \times [l_{4,5} + l_{5,6} + l_{6,7} - (l_{4,8} + l_{8,9} + l_{9,10} + l_{10,11})] + \Delta\phi_{OE} \end{aligned} \quad (11)$$

where $\Delta\phi_{OE}$ represents the constant difference in phase shift produced by the optical element in each path. We can also find the sum of the phases:

$$\begin{aligned} \Sigma\Psi &= \Psi_1 + \Psi_2 = k \times (L_{c1} + L_{c2}) + 2\phi_{mit} \\ &= k \times [2 * (l_{1,2} + l_{2,3} + l_{3,4}) + l_{4,5} + l_{5,6} + l_{6,7} + l_{4,8} + l_{8,9} + l_{9,10} + l_{10,11}] + 2\phi_{mit} \end{aligned} \quad (12)$$

where ϕ_{mit} is the phase of the laser prior to hitting the first BS. By adjusting PZT-2 we are able to control L_{c2} directly, allowing us to adjust the value of $\Delta\Psi$. This phase difference is independent of $[l_{1,2} + l_{2,3}]$, which is controlled by PZT-1a. However, it is clear that $\Sigma\Psi$ does depend on these lengths (i.e. $[l_{1,2} + l_{2,3}]$). In this way we can scan this phase (i.e. $\Sigma\Psi$), thus varying α , while separately adjusting $\Delta\Psi$ to maximize $|\beta|$. Nevertheless, it is clear that varying $\Delta\Psi$ will also change $\Sigma\Psi$, as they both depend on $[l_{4,8} + l_{8,9}]$. For this reason, to vary β without affecting α it is necessary to have another PZT, denoted PZT-1b (shown in Fig. 2), as explained below.

We define Δl_{pzt} as the matching change in $l_{4,8}$ and $l_{8,9}$ produced by the displacement of PZT-2 away from its static point. Similarly, we can also define Δl_{ref} as the matching change in $l_{4,5}$ and $l_{5,6}$ due to the displacement of PZT-1b. This gives us:

$$\begin{aligned} l_{4,8} + l_{8,9} &= l'_{4,8} + l'_{8,9} + \Delta l_{pzt} \\ l_{4,5} + l_{5,6} &= l'_{4,5} + l'_{5,6} + \Delta l_{ref} \end{aligned} \quad (13)$$

where $l'_{n,m}$ represents the path length when the relevant PZT is at its static point. We can now write:

$$\begin{aligned} \Delta\Psi &= k \times \left[l'_{4,5} + l'_{5,6} + l_{6,7} - (l'_{4,8} + l'_{8,9} + l_{9,10} + l_{10,11}) + (\Delta l_{ref} - \Delta l_{pzt}) \right] + \Delta\phi_{OE} \\ \Sigma\Psi &= k \times \left[2 * (l_{1,2} + l_{2,3} + l_{3,4}) + l'_{4,5} + l'_{5,6} + l_{6,7} + l'_{4,8} + l'_{8,9} + l_{9,10} + l_{10,11} + (\Delta l_{ref} + \Delta l_{pzt}) \right] + 2\phi_{init} \end{aligned} \quad (14)$$

From Eq. (14) it is clear that by setting $\Delta l_{ref} = -\Delta l_{pzt}$ we can get rid of the PZT-2 dependence of $\Sigma\Psi$ while doubling it in $\Delta\Psi$:

$$\begin{aligned} \Delta\Psi &= k \times \left[l'_{4,5} + l'_{5,6} + l_{6,7} - (l'_{4,8} + l'_{8,9} + l_{9,10} + l_{10,11}) - (2\Delta l_{pzt}) \right] + \Delta\phi_{OE} \\ \Sigma\Psi &= k \times \left[2 * (l_{1,2} + l_{2,3} + l_{3,4}) + l'_{4,5} + l'_{5,6} + l_{6,7} + l'_{4,8} + l'_{8,9} + l_{9,10} + l_{10,11} \right] + 2\phi_{init} \end{aligned} \quad (15)$$

Mechanically this means that PZT-1b has to be programmed to move the exact same distance as PZT-2, but in the opposite direction. This can be achieved using a feed-forward system where an inverted version of the bias signal applied to PZT-2 is sent to PZT-1b.

The PID system that controls PZT-2 receives its feedback from MZI_PD. The phase difference between the two path lengths in the MZI can be written as $\Delta\Psi_{MZI} = \Psi_{control} - \Psi_{static}$, where

$$\begin{aligned} \Psi_{control} &= k \times (l_{3,4} + l'_{4,8} + l'_{8,9} + l_{9,13} + \Delta l_{pzt}) \\ \Psi_{static} &= k \times (l_{3,12} + l_{12,13}) \end{aligned} \quad (16)$$

so that

$$\Delta\Psi_{MZI} = k \times \left[l_{3,4} + l'_{4,8} + l'_{8,9} + l_{9,13} + \Delta l_{pzt} - (l_{3,12} + l_{12,13}) \right] \quad (17)$$

This means that to lock the PID to a specific phase at MZI_PD ($\Delta\Psi_{MZI}$) we will have a set value of Δl_{pzt} , which will also lock $\Delta\Psi$. We can vary this value by use of a bias voltage that is added to the output of the PID controller [24].

As was previously shown, PZT-1a allows us to adjust the value of Ψ_1 and Ψ_2 simultaneously without changing $\Delta\Psi$. By continuously running a ramp signal at some frequency ω_s on this PZT, we can scan over a wide range of phases. By applying a Low Pass Filter (LPF) to the detected signal with a cutoff frequency $\omega_c \ll \omega_s$ we can get rid of the α term in Eq. (6), leaving only the cross-correlation signals in our final HOC output:

$$\begin{aligned} S_f &= \beta^* T_3 + \beta T_4 \\ &= \beta^* [H_2(x,y) \odot H_1(x,y)] + \beta [H_1(x,y) \odot H_2(x,y)] \end{aligned} \quad (18)$$

This is the ideal way to operate the HOC. However, because the phase scan operates in the time domain, this method requires that all six signals (A_j, B_j , and C_j) be detected simultaneously with six FPA's, and without shutters, which greatly increases the complexity of the system. As such, we did not implement the scanning segment of the PSS for the demonstration reported here. It should be noted that it is still possible to see the results of a correlation without washing out the α term, but one must be careful to distinguish between the correlation and convolution terms.

One way to reach the maximum value of $|\beta|$ for an unknown α is to run a series of known matched images through the HOC at varying bias voltages. This works as follows. One image is set as both the Reference and Query inputs. The HOC then runs a correlation, for a particular bias voltage. This will yield a match at the output of the HOC. The bias voltage is then changed within the range of operation of the PZT, repeating the correlation. The result will again be a match, but the overall output intensity will have either increased or decreased. The bias voltage is changed so as to look for the maximum intensity. This process is repeated, changing the bias in progressively smaller steps until the maximum output intensity is found.

3. POLAR MELLIN TRANSFORM IN THE HOC

Due to the properties of the FT and lenses, the detection of a FT'd optical signal will be shift invariant. However, changes to the scale and rotation of the images will alter the scale and rotation of the FT, thus preventing the HOC

from achieving a match. To counteract this, we can instead compare images that have been pre-processed via the use of the Polar Mellin Transform (PMT).

Because the PMT is, by definition, in log-polar coordinates, two identical images with different rotations will present the same PMT with a shift in the θ coordinate corresponding to the relative rotation angle between them. Similarly, any change in scale will manifest as a shift in the log-radial coordinate ρ . By performing the PMT we are essentially converting any rotation and scale changes into translational shifts. Given that the established HOC architecture is inherently shift invariant and that the PMT is very closely related to the FT, it is thus well suited for adding rotation and scale invariance into the HOC architecture, as explained in detail in [20].

The steps to obtain the PMT in an optoelectronic system are as follows: 1- Find the FT of the image. 2- Determine the amplitude of the FT. (2a- Determine the intensity of the FT. 2b- Find the square root of the intensity). 3- Perform circular DC blocking. 4- Map polar coordinates into a rectilinear plane where x and y correspond to the r and θ axes. 5- Transform radial coordinate to the logarithm of the ratio of the radial coordinate and a reference length.

Steps 1 and 2a can be performed using a laser, an SLM, an FT lens, and an FPA. In this setup we used a single arm of our existing HOC architecture with the PSS shutter (S1) closed. Steps 2b-5 are then performed by a computer. The resulting PMT image is then used as an input to the HOC. By using a PMT image as a reference and converting a query image into its PMT, the HOC is able to find the correlation of the two original images in a shift, scale, and rotation invariant manner.

Given that all real digital images are composed of positive integer values, their FT will always contain a high value at the center (DC). The transformation from $\{x, y\}$ to $\{\rho, \theta\}$ of such an image will produce an output that has a non-zero value for $\rho=0$. It is impossible to transform this point to the log-polar domain. To avoid this, we cut a small hole in the intensity profile of the FT at DC prior to performing the polar coordinate transformation. This is called circular DC blocking [20]. It is important that the hole be small enough not to erase important information from the non-DC area of the FT. However, making the hole very small requires high pixel density. A convenient compromise is to use a small hole of a constant size for all images.

4. EXPERIMENTAL RESULTS

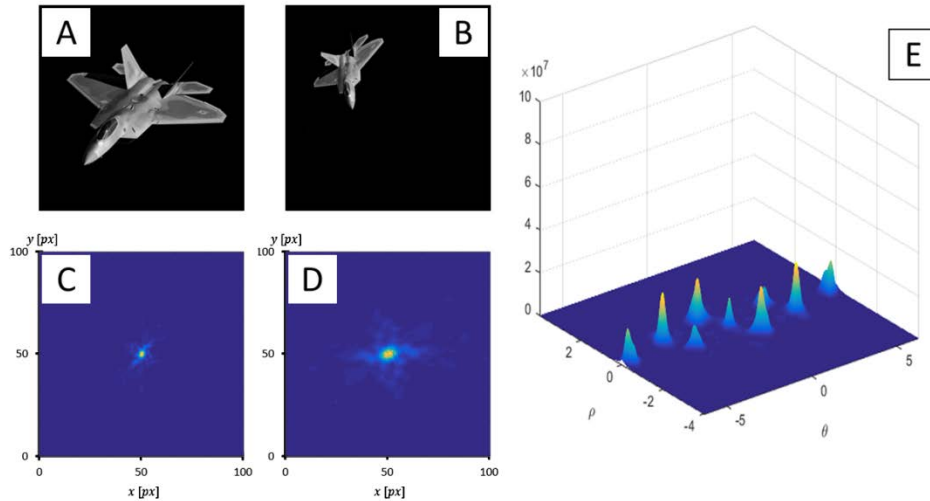


Fig 4. HOC results without the PMT. **A:** Reference Input. **B:** Query Input. **C:** Measured FT of A. **D:** Measured FT of B. **E:** Output scaled to the intensity of a known match.

For this experiment, a grayscale image of an F-22 Raptor fighter jet was chosen for its excellent contrast, unique shape, and real-world value. Prior to running the experiment, the HOC was calibrated to its optimum bias voltage by using the method described in Section 2.4.

The original reference image is shown in Fig. 4(A). The query image shown in Fig. 4(B) has been shifted and is scaled by a factor of 0.5 with a rotation of 48.25° counterclockwise with respect to the reference. The detected FT's of these two images are shown in Figs. 4(C) and 4(D) respectively. Because the query image is scaled, its FT is

larger than the reference while also presenting a rotation. Due to these two factors, the HOC was unable to detect a match, producing an almost flat output signal $|s_f|^2$ in Fig. 4(E).

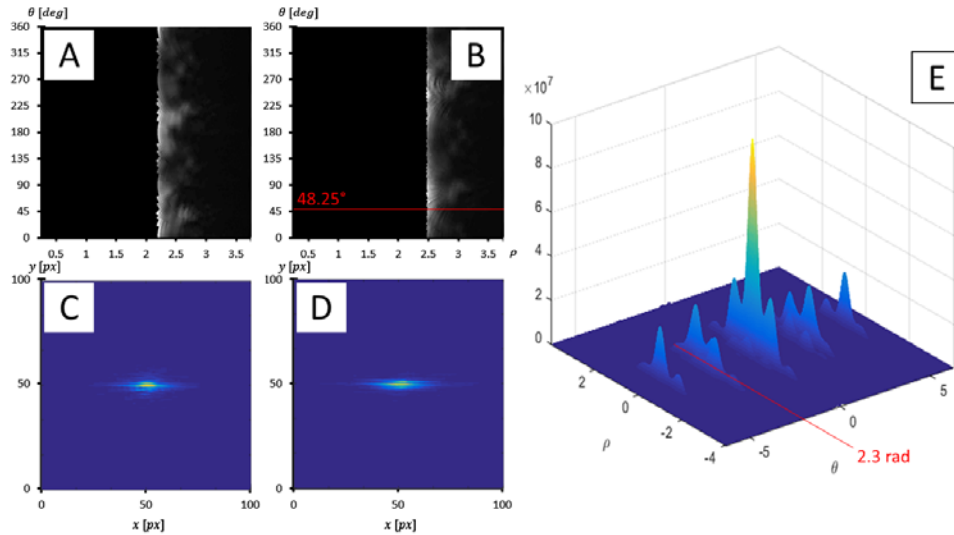


Fig 5. HOC results with the PMT. **A:** Reference PMT Input (converted from 4.C). **B:** Query PMT Input (converted from 4.D). **C:** Detected FT of A. **D:** Detected FT of B. **E:** Output scaled to the intensity of a known match.

Figures 4.C and 4.D were then used as FT intensities in the PMT conversion process described in Section 3. The PMT'd images are shown in Figs. 5(A) and 5(B), where the vertical axis represents θ and the horizontal axis represents ρ . Using these PMT images as new inputs to the HOC, their FT's (figs. 5(C) and 5(D)) were detected. In these new FT's, the scale and rotation of the query image with respect to the reference is no longer visible. This is corroborated by the output $|s_f|^2$ shown in Fig. 5(E) which shows a clear peak that is ~ 7 times larger than that of Fig. 4(E), indicating a successful correlation. On Fig. 5(B) we have added a red horizontal line that marks the value of θ that corresponds to $\theta = 0$ in Fig. 5(A). This line shows the translational shift of the PMT caused by the rotation of the original query image. The section of the PMT that corresponds to the top of Fig. 5(A) has looped around to be under this red line.

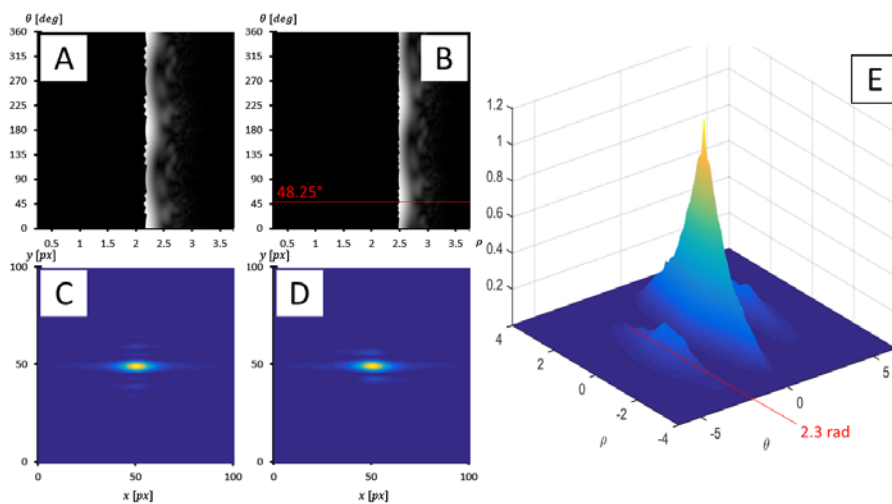


Fig 6. HOC simulation with the PMT. All images are simulated. **A:** Reference PMT Input (from 4.A). **B:** Query PMT Input (from 4.D). **C:** 2-D Fast Fourier Transform (FFT) of A. **D:** FFT of B. **E:** Output normalized to 1.

To complement these results, a simulation using the same input images was run. This is shown in Fig. 6, corresponding to the ideal reference PMT, ideal query PMT, their ideal FT's, and the simulated HOC output $|S_f|^2$. In Fig. 6(B) we have added a similar red line to the one in Fig. 5(B), this time corresponding to $\theta=0$ in Fig. 6(A). By measuring the distance in pixels between the bottom of the PMT and the red line, recalling that the full vertical axis represents 360° , we can estimate the rotation of the query image to be $\approx 48^\circ$, which is close to the real rotation of 48.25° . Similarly, the distance between the central peak of the output signal and the two lateral peaks in Figs. 5(E) and 6(E) has been marked with a red line. This is located at $\theta=2.3$ radians, which is equivalent to a rotation of $(\pi-\theta)=48.22^\circ$.

5. USING HOLOGRAPHIC MATERIALS FOR LARGE DATABASE STORAGE

While the HOC is capable of performing ultra-fast correlations, it is still limited by the speed of its electronic components. In particular the currently available commercial SLMs present the largest barrier, generally having refresh rates on the order of milliseconds. To overcome this, it is possible to replace the reference SLM with a database stored in a thick holographic substrate, which can have a very large storage capacity and can be read at high speeds through optical means, making it ideal for this application. This is due to the fact that it is also possible to store a large numbers of images in a single spatial location in a thick holographic substrate through angle multiplexing.

There are two types of holographic memory devices (HMD's); reflection and transmission. Reflection holograms have their output on the same side as the input, and transmission holograms present their output on the opposite side of the HMD. We will refer solely to transmission holograms for the purposes of this paper. In general, HMD's are created by interfering an information-carrying beam with a separate reference beam in a holographic medium. The medium is made of a photosensitive material that reacts to the lasers, changing its chemical properties according to the intensity of the interference pattern. This can be repeated at different locations on the HMD, or on the same location by varying the interference angle. The latter option is known as angle multiplexing and allows for high-density data storage. The number of images that can be written to a single spatial location is known as the M-number (M/#) [25]. This number depends on the medium, the photosensitive dye, the power of the beams, and the thickness of the HMD. Thicker devices allow for a higher M/#, but are more sensitive to angle changes and so require more precise control mechanisms. Once the HMD has been exposed to the interference pattern, it is cured and bleached in order to lock in the holograms and prevent accidental overwriting.

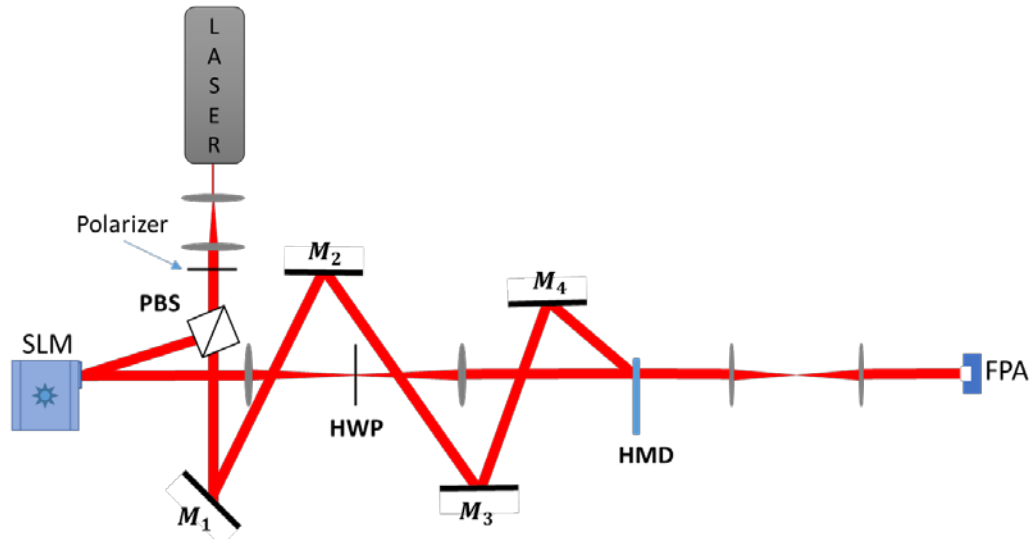


Fig 7. Setup for writing holograms on the HMD. This same setup can be used to read holograms by removing the SLM and its corresponding beam.

To read a hologram, the finished HMD is placed in the path of a reading beam that is identical to the reference beam. The stored image will be reproduced in the direction of the original (writing) image beam. If multiple angle

multiplexed images exist, we can vary the angle of the reading beam in order to read each separate image at its respective angle.

We have developed an HMD for 532 nm lasers using PQ dye on a PMMA substrate. PQ:PMMA is first created in a liquid form and poured into a mold of arbitrary shape, in our case a 2 mm thick by 52 mm diameter circle. After curing into a solid, the HMD is placed in a writing setup shown in Fig. 7. Here, a laser beam is first passed through a spatial filter to produce a Gaussian beam. The beam is then split into two parts using a polarized beam splitter (PBS), where a polarizing filter allows us to select the percentage of light that gets split. One arm is used as a reference beam and the other as an image beam, the latter of which reflects off of an SLM and passes through a 4f system to reach the HMD. It should be noted that the image beam also passes through a half wave plate (HWP) in order to change its polarization to match the reference beam. The reference beam is redirected towards the HMD at a set angle. Angle multiplexing can be achieved by rotating mirrors M2 and M3, but was not done for this experiment. The HMD was designed to be rotated along the beam's x-y plane in order to reach multiple writing locations. To minimize light-contamination of neighboring writing locations, a mask (not shown) of the same size as the image beam was placed just before the HMD.

Once the hologram has been written, it can be accessed using the same setup, but without the image beam. Alternatively, any setup can be used to read the HMD as long as the input angle of the reading beam corresponds to that of the original writing beam. A 4f system placed after the HMD allows us to capture the hologram on an FPA with minimal losses. Fig. 8 shows a typical one of many images that were written and read from a 2mm thick hologram. The laser was set at a power of 1.5 W over a 1" wide beam, with an exposure time of 100 seconds. The reference and image beams were split at 50/50 power.

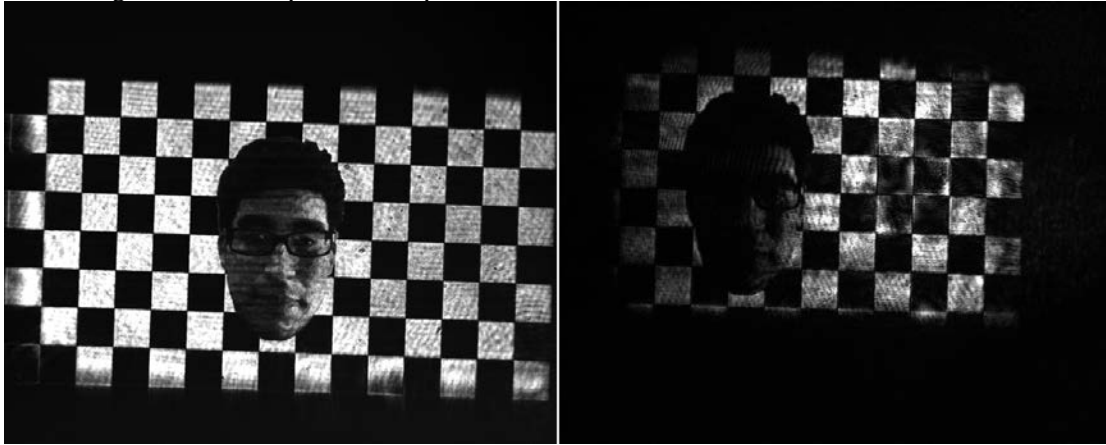


Fig 8. A typical image written (left) and read (right) from a 2mm thick HMD. The laser was set at a power of 1.5 W over a 1" wide beam, with an exposure time of 100 seconds. The reference and image beams were split at 50/50 power.

It is clear from Fig. 8 that, while the HMD was able to store the image, some information was lost. This is likely due to imperfections in the HMD itself as well as the writing/reading system. We are currently working to minimize these distortions, and implement an automated system for recording a larger number of images in a single HMD, using a combination of spatial and angular multiplexing.

6. CONCLUSIONS AND OUTLOOK

We have demonstrated that an HOC built using commercially available components and incorporating the PMT is able to find a match in a shift, scale, and rotation invariant manner, yielding an output that is ~7 times larger when a match is found vs when it is not found (without the PMT). Furthermore, the relative rotation of the query image with respect to the reference image in a match can be found in the output signal by measuring the distance from the central peak to one of the two lateral peaks. We have also shown that the behavior of the PMT-augmented HOC aligns with the theory by presenting simulated results that correspond to our experiment. The development of an HMD that is capable of storing a large database of images that have already undergone the PMT process is essential for the HOC. We have shown that thick PQ:PMMA holographic substrates are well suited for realizing such an HMD.

7. FUNDING

The work reported here was funded by the Air Force Office of Scientific Research (AFOSR) under grant number FA9550-18-01-0359.

8. REFERENCES

1. A. Vander Lugt, "Signal detection by complex spatial filtering," *IEEE Trans. Inf. Theory* **10**, 139–145 (1964).
2. A. Heifetz, J. T. Shen, J.-K. Lee, and M. S. Shahriar, "Translation-invariant object recognition system using an optical correlator and a super-parallel holographic random access memory," *Opt. Eng.* **45**, ID 025201 (2006).
3. A. Heifetz, G. S. Pati, J. T. Shen, J. Lee, M. S. Shahriar, C. Phan, and M. Yamamoto, "Correlator using video-rate compatible photorefractive polymer," *Appl. Opt.* **45**, 6148–6153 (2006).
4. Q. Tang and B. Javidi, "Multiple-object detection with a chirp-encoded joint transform correlator.," *Appl. Opt.* **32**, 5079–5088 (1993).
5. J. Khoury, M. Cronin-golomb, P. Gianino, and C. Woods, "Photorefractive two-beam-coupling nonlinear joint-transform correlator," *J. Opt. Soc. Am. B Opt. Phys.* **11**, 2167–2174 (1994).
6. B. Javidi, J. Li, and Q. Tang, "Optical implementation of neural networks for face recognition by the use of nonlinear joint transform correlators," *Appl. Opt.* **34**, 3950–3962 (1995).
7. F. T. S. Yu and X. J. Lu, "A real-time programmable joint transform correlator," *Opt. Commun.* **52**, 10–16 (1984).
8. M. S. Shahriar, R. Tripathi, M. Kleinschmit, J. Donoghue, W. Weathers, M. Huq, and J. T. Shen, "Superparallel holographic correlator for ultrafast database searches," *Opt. Lett.* **28**, 525–527 (2003).
9. F. Lei, M. Iton, and T. Yatagai, "Adaptive binary joint transform correlator for image recognition," *Appl. Opt.* **41**, 7416–7421 (2007).
10. D. A. Gregory, J. A. Loudin, and H.-K. Liu, "Joint transform correlator limitations," in *Proc. SPIE 1053, Optical Pattern Recognition* (SPIE, 1989), pp. 198–207.
11. B. Javidi and C.-J. Kuo, "Joint transform image correlation using a binary spatial light modulator at the Fourier plane," **27**, 663–665 (1988).
12. M. S. Monjur, S. Tseng, R. Tripathi, J. J. Donoghue, and M. S. Shahriar, "Hybrid optoelectronic correlator architecture for shift-invariant target recognition," *J. Opt. Soc. Am. A* **31**, 41–47 (2014).
13. M. S. Monjur, S. Tseng, M. F. Fouda, and S. M. Shahriar, "Experimental demonstration of the hybrid optoelectronic correlator for target recognition," *Appl. Opt.* **56**, 2754–2759 (2017).
14. D. Casasent and D. Psaltis, "Position, rotation, and scale invariant optical correlation," *Appl. Opt.* **15**, 1795–1799 (1976).
15. D. Casasent and D. Psaltis, "Scale invariant optical correlation using Mellin transforms," *Opt. Commun.* **17**, 59–63 (1976).
16. D. Casasent and D. Psaltis, "New optical transforms for pattern recognition," *Proc. IEEE* **65**, 77–84 (1977).
17. D. Asselin and H. H. Arsenault, "Rotation and scale invariance with polar and log-polar coordinate transformations," *Opt. Commun.* **104**, 391–404 (1994).
18. D. Sazbon, Z. Zalevsky, E. Rivlin, and D. Mendlovic, "Using Fourier/Mellin-based correlators and their fractional versions in navigational tasks," *Pattern Recognit.* **35**, 2993–2999 (2002).
19. J. Gamboa, M. Fouda, and S. M. Shahriar, "Demonstration of the hybrid opto-electronic correlator for shift, scale, and rotation invariant target recognition," *Opt. Express* **27**, 16507–16520 (2019).
20. M. S. Monjur, S. Tseng, R. Tripathi, and M. S. Shahriar, "Incorporation of polar Mellin transform in a hybrid optoelectronic correlator for scale and rotation invariant target recognition," *J. Opt. Soc. Am. A* **31**, 1259–1272 (2014).
21. G. W. Li, S. J. Huang, H. S. Wu, S. Fang, D. S. Hong, T. Mohamed, and D. J. Han, "A Michelson interferometer for relative phase locking of optical beams," *J. Phys. Soc. Japan* **77**, ID 024301 (2008).
22. B. W. Shiau, T. P. Ku, and D. J. Han, "Real-time phase difference control of optical beams using a mach-zehnder interferometer," *J. Phys. Soc. Japan* **79**, ID 034302 (2010).
23. M. Lu, H. C. Park, E. Bloch, L. A. Johansson, M. J. Rodwell, and L. A. Coldren, "An integrated heterodyne optical phase-locked loop with record offset locking frequency," *Opt. Fiber Commun. Conf. OSA Tech. Dig.* ID Tu2H.4 (2014).

24. Because the PZT is an electro-mechanical device, it requires a voltage source and a control circuit that introduce electrical noise into the system. A PID controller allows the PZT to maintain a more stable position. However, PID systems require a feedback.
25. H. N. Yum, P. R. Hemmer, R. Tripathi, J. T. Shen, and M. S. Shahriar, "Demonstration of a simple technique for determining the M/# of a holographic substrate by use of a single exposure," *Opt. Lett.* **29**, 1784 (2004).